2025 MANDALAY EARTHQUAKE

RESEARCH ARTICLE

Bimaterial effect and favorable energy ratio enabled supershear rupture in the 2025 Mandalay earthquake

Liuwei Xu[1], Lingsen Meng[1]*, Zhang Yunjun[2,3], Yanchen Yang[4,5], Yidi Wang[2,3], Changyang Hu[2,3], Huihui Weng[6], Wenbin Xu[7], Elizabeth Su[1], Chen Ji[8]

Joint seismic and geodetic analyses revealed that the 2025 moment magnitude (M_w) 7.8 Mandalay, Myanmar, earthquake ruptured ~510 km of the Sagaing fault, with a sustained supershear rupture extending ~450 km on the southern branch. Far-field Mach waves and near-field ground motion confirmed the supershear nature. This exceptionally long supershear rupture caused building collapse and soil liquefaction, as observed in satellite imagery, offering insights into the damage potential of such ruptures in urban areas. Sustained supershear propagation was facilitated by the fault's linear geometry, prolonged interseismic quiescence, favorable energy ratio, and pronounced bimaterial contrasts across the fault interface. These findings underscore the roles of fault structure, stress accumulation, and material contrasts in governing rupture dynamics, demonstrating that large-scale supershear propagation can occur in interplate continental fault systems.

At 12:51 p.m. local time on 28 March 2025, a moment magnitude (M_w) 7.8 earthquake struck near the city of Mandalay, Myanmar. Situated at the junction of three tectonic plates—the Indian (IN), Eurasian (EU), and Burma (BU) plates (*1, 2*)—Myanmar is subject to high seismicity. The central longitudinal axis of the country, home to both the major economic center of Mandalay and the political capital NayPyiDaw, coincides with the boundary between the BU and EU plates (Fig. 1A). The right-lateral strike-slip Sagaing fault, which marks the boundary, spans ~1400 km and accommodates a relatively high slip rate of ~20 mm/year (*3*, *4*). In the 20th century, the Sagaing fault generated at least seven magnitude (M) ≥ 7 earthquakes along different segments (Fig. 1A), with the exception of a seismic gap between Mandalay and NayPyiDaw (Fig. 1A) (*2*, *5*). The 2025 Mandalay earthquake ruptured this long-standing seismic gap. The epicenter was located near Mandalay, and early reports indicated a bilateral, north-south (N-S)–oriented rupture (*6*). According to data compiled by the Democratic Voice of Burma, the earthquake resulted in 4355 confirmed fatalities, 210 people reported missing, and 7830 injured.

To obtain timely and comprehensive fault rupture details about the earthquake, we collected global seismic data and applied the slowness-enhanced back-projection (SEBP) method (*7*). SEBP enabled us to resolve the spatiotemporal evolution of high-frequency (HF) radiators along the fault during the mainshock. We also derived coseismic ground deformation using synthetic aperture radar (SAR) and optical imagery from the Sentinel-1, LuTan-1, ALOS-2, and Sentinel-2 satellites. These deformation observations, in combination with global and local seismic datasets, were jointly inverted through finite fault inversion (FFI) (*8*, *9*) to reconstruct the slip distribution, rupture history, and slip vectors across the fault. Our integrated analysis of SEBP and joint FFI results revealed that the earthquake ruptured the subvertical Sagaing fault in a bilateral manner along the N-S direction. The northern branch rupture was relatively minor, with an approximate length of 60 km and an average rupture speed of 0.9 km/s. By contrast, the southern branch exhibited an unusually fast rupture, propagating ~450 km at a speed of 5.0 km/s, exceeding the local shear wave velocity and therefore classifying it as a supershear rupture. We confirmed the supershear nature of the southern segment by identifying Mach waves and Mach cones in the seismic wavefield and by analyzing ground motions recorded at a near-fault station.

Owing to the ongoing civil conflict in Myanmar, field investigations and postevent damage assessments have been substantially constrained. To address this limitation, we generated damage proxy maps (DPMs) and analyzed them in conjunction with other satellite radar imagery. DPMs highlight regions where the radar backscattering characteristics changed anomalously relative to their typical background variation, indicative of potential structural damage (*10*, *11*). Optical satellite images revealed building collapses in urban areas and widespread secondary hazards (e.g., soil liquefaction, landslides), which aligned with regions of high DPM values. This study offers a detailed characterization of the prolonged and devastating earthquake, providing a set of observations that can serve as a reference for postevent hazard assessment.

Rupture kinematics resolved by SEBP and joint FFI

The SEBP analysis revealed an asymmetrical bilateral rupture propagating in the N-S direction. The HF radiators closely followed the surface trace of the Sagaing fault (Fig. 1A and figs. S1 to S9). All three arrays consistently indicated a fast rupture speed of 4.8 to 5.0 km/s on the southern branch (Fig. 1C; figs. S2B, S4B, and S6B; and movies S1 to S3). The length of the southern rupture segment was ~450 km. The speed substantially exceeded the local shear wave speed in the crust above depths of 20 km (2.5 to 3.7 km/s; fig. S10 and table S1) (*5*), suggesting supershear rupture. By contrast, the northern branch exhibited a shorter and slower rupture. Based on SEBP results, the northern rupture extended ~60 km with an estimated average speed of 0.9 km/s (*12*). The rupture speeds resolved by the three arrays showed greater variability, ranging from 0.9 to 1.7 km/s (figs. S2B, S4B, and S6B). This variation likely reflects uncertainties introduced by the relatively weak HF radiation from the northern branch, attributable to its slower rupture speed and interference from the southern branch's signal (*13*). We validated the speed measurements by applying back-projection to synthetic seismograms generated by a bilateral model with a subshear northern branch and a supershear southern branch (*12*) (figs. S11 to S13). The recovered southern speeds were 8 to 20% lower than the input value, whereas those of the northern branch were underestimated by 30% (figs. S11 and S12). Although such underestimation may be less pronounced in real earthquake back-projection, it suggests greater uncertainty in back-projection results for the northern branch. Nevertheless, the synthetic back-projection confirmed the supershear nature of the southern rupture and the subshear nature of the northern one.

The joint FFI results indicated that the rupture was predominantly right-lateral strike-slip (Fig. 2C and movie S4). The coseismic slip distribution aligned well with the HF radiators (Fig. 1C); north of the epicenter, slip extended ~60 km, whereas the southern rupture extended

[1]Department of Earth, Planetary and Space Sciences, University of California Los Angeles, Los Angeles, CA, USA. [2]National Key Laboratory of Microwave Imaging, Aerospace Information Research Institute, Chinese Academy of Sciences, Beijing, China. [3]School of Electronic, Electrical and Communication Engineering, University of Chinese Academy of Sciences, Beijing, China. [4]National Engineering Research Center for Remote Sensing Satellite Applications, Aerospace Information Research Institute, Chinese Academy of Sciences, Beijing, China. [5]School of Resources and Environment, University of Chinese Academy of Sciences, Beijing, China. [6]State Key Laboratory for Mineral Deposits Research, School of Earth Sciences and Engineering, Nanjing University, Nanjing, China. [7]School of Geoscience and Info-Physics, Central South University, Changsha, China. [8]Department of Earth Science, University of California, Santa Barbara, Santa Barbara, CA, USA. ***Corresponding author. Email: lsmeng@g.ucla.edu**

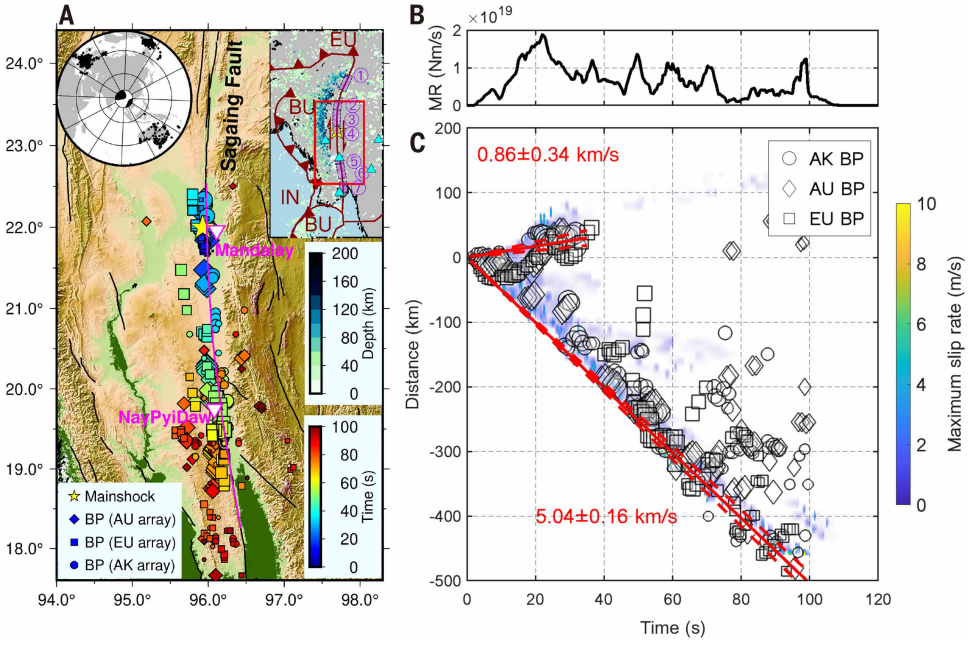

Fig. 1. Overview map and rupture process. (**A**) Back-projection (BP) results and active faults (black lines). (*2*). Colored symbols represent HF radiators imaged by three seismic arrays (see legend). Symbol size is proportional to beam power, and color indicates rupture time relative to the mainshock origin time (the lower legend). White triangles denote the major cities along the Sagaing fault. The magenta line denotes the surface rupture identified according to the ground deformation. (Inset, upper left) Locations of the three arrays. (Inset, upper right) The regional tectonic map. Colored dots indicate historical seismicity from 1 January 1990 to 3 April 2025, color-coded by hypocenter depth (the upper legend). Dark red lines mark plate boundaries (*1*, *2*). The red box highlights the source region shown in the main image. Cyan triangles denote strong motion stations. Purple bars denote rupture zones of historical *M* 7 earthquakes in the 20th century, with event names and magnitudes listed in table S3 (*2*). BU, Burma plate; IN, Indian plate; EU, Eurasian plate. (**B**) Moment rate function illustrating the temporal evolution of seismic moment release. (**C**) Rupture velocity from SEBP and comparison to the FFI. Symbols mark the timing and location of HF radiators. Locations are shown as along-fault distance relative to the hypocenter, with positive values to the north and negative values to the south. The red solid line indicates the best-fit rupture front, with standard deviation (±1 σ) outlined by dashed lines. The background colormap represents the maximum slip rate at each along-strike position from the FFI.

~450 km. Near the hypocenter, the fault dips 65° to the east, whereas along the southern branch, it steepens to 80° [see also (*12*)]. Slip was concentrated at shallow depths: About 75% of the seismic moment was released between 0- and 15-km depth, with a peak slip of ~7.9 m. The total seismic moment was 6.37×10^{20} N·m, corresponding to a moment magnitude of M_w 7.8. Most of the moment release occurred within the first 100 s (Fig. 1B). Rupture duration exceeded the typical value predicted by the global scaling relationship [~40 s (*14*)] but was comparable to that of some M_w 7.8 strike-slip events, such as the 2001 Kunlun (*15*), 2013 Scotia (*16*), and 2023 Türkiye earthquakes (*17*). Our model successfully reproduced static displacements observed in SAR and optical satellite data (figs. S14 to S16) and provided good fits to teleseismic and local strong-motion recordings (figs. S17 to S22), including at station NPW, located just 2 to 3 km from the fault (figs. S21 and S22). Nine additional inversions using different initial models yielded minor standard deviations in both objective function values and coseismic slip distributions [(*12*); fig. S23], confirming the robustness of our solution.

In the back-projection images, we observed that the HF radiators extended farther along the southern branch than mapped surface fault traces (Fig. 1A). The slip model revealed that the southern segment between 420 and 460 km hosted coseismic slip that did not reach the surface, thereby accounting for the discrepancy in rupture extent. Additionally, several southern radiators observed after 90 s exhibited a westward spatial bias relative to the fault trace, likely caused by coda-wave contamination during the rupture's terminal phase. The distribution of northern HF radiators was consistent with both the mapped surface traces and the slip model after calibration (*12*). The northern surface rupture terminated near ~22.5°N, coinciding with the southern edge of a M_w 6.8 strike-slip earthquake in 2012 (fig. S24) (*18*). This termination may reflect prior stress release from the 2012 event that impeded rupture propagation.

Aftermath estimation by satellite damage proxy maps

The DPMs derived from Sentinel-1A satellite imagery have served as a key tool for systematically assessing the mainshock and its impacts in the absence of on-ground postevent damage assessments (Fig. 3) (*10*–*12*, *19*). We found that areas exhibiting high DPM values closely align with the spatial orientation of fault traces, consistently forming a 2- to 3-km-wide zone along the fault (Fig. 3 and fig. S25). This pattern helps delineate the extent of off-fault damage and reveals widespread surface destruction beyond the primary rupture zone. By integrating building footprint data with hazard models from the US Geological Survey (USGS) and using a causal Bayesian network to model seismic multihazards and their impacts (*12*, *20*), we generated three high-resolution (45 m) hazard probability maps for building damage, liquefaction, and landslides, respectively (Fig. 3 and figs. S26-S28). Building collapses were observed in Mandalay, with high landslide potential identified at Sagaing Hill and high soil liquefaction potential in the Irrawaddy floodplain and the city's southeastern areas (Fig. 3). These findings underscore the multiscale mechanisms underlying seismic impacts and demonstrate the effectiveness of satellite-based seismic multihazard and impact assessments, particularly in regions where on-the-ground access is limited.

Validation of supershear rupture

We further validated the southern supershear rupture using surface wave observations. As proposed by (*21*), a supershear rupture exhibits distinct characteristics in the far-field surface wave field: within specific regions, waves from different parts of the rupture arrive simultaneously and interfere constructively, simplifying the Rayleigh and Love waveforms. This results in a high degree of similarity between the waveforms of the large supershear rupture and those of a smaller, colocated event (hereinafter referred to as an empirical Green's function, EGF). These regions of constructive interference are known as Mach cones, with the recorded surface waves referred to as Mach waves, and the angles between the Mach cones and the rupture direction termed Mach angles (*12*). We collected 76 Rayleigh waveforms to identify Mach waves and cones. To minimize surface wave dispersion, seismograms were bandpass filtered to 15 to 25 s following (*21*, *22*). The EGF was a M_w 5.1 event that occurred north of the mainshock epicenter with a similar focal mechanism (EGF 2, table S2 and fig. S24). We quantified waveform similarity using standard cross-correlation

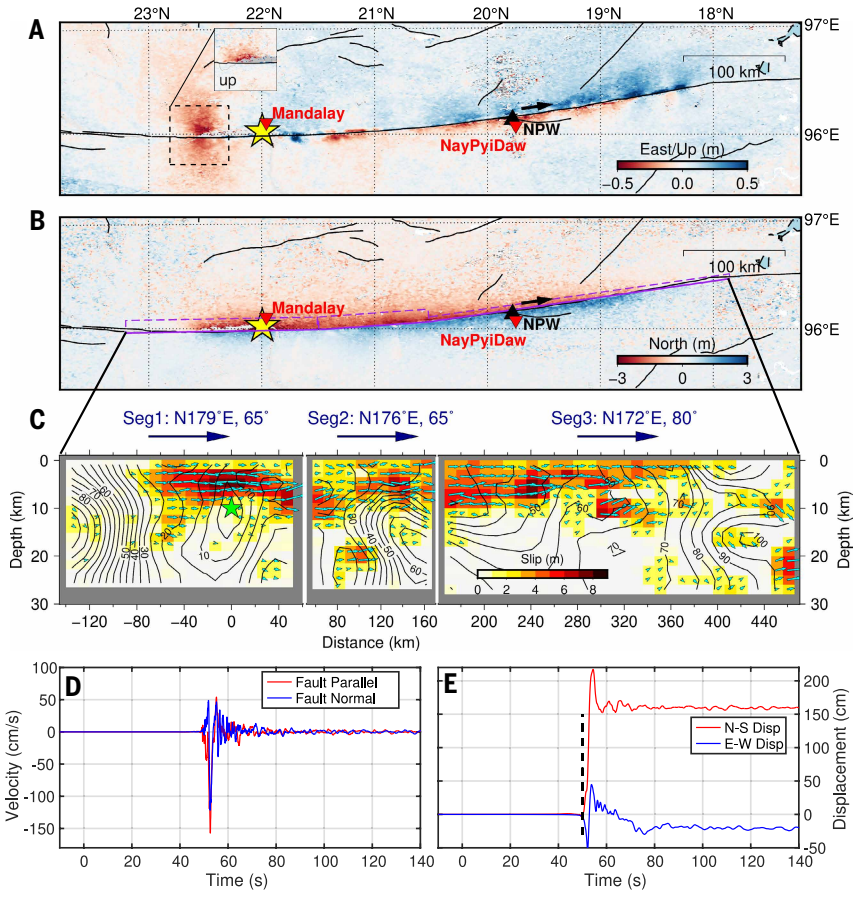

Fig. 2. Ground deformation and slip model. (**A**) East-west (E-W) ground deformation. The zoomed-in inset presents the vertical ground deformation with full coverage shown in fig. S32C. Inverted triangles denote major cities along the fault. The black triangle indicates the seismic station GE.NPW, and the arrow shows the FP direction (N172°E). The deformation reference point is set at (N20.0°, E94.6°), outside the figure extent. (**B**) N-S ground deformation. Purple boxes outline the boundaries of the fault model used in the joint FFI, with solid lines denoting the upper fault boundaries and dashed lines representing other boundaries. (**C**) Spatial distribution of final slip (color scale), rupture initiation time (black contours in seconds), and rake angle (cyan arrows) along the fault. Strike and dip angles for each fault segment are labeled at the top. (**D**) Comparison of FP (red) and FN (blue) velocity seismograms recorded at GE.NPW. Waveforms are obtained by integrating the raw acceleration data and removing baseline drifts. The time axis is referenced to the earthquake origin time (28 March 2025, 06:20:52 UTC). (**E**) Ground displacement time series at GE.NPW. N-S (red) and E-W (blue) components are shown. The bold dashed line marks the onset of substantial ground deformation, occurring 50 s after the origin time. Displacements are calculated by integrating the velocity seismograms and applying drift corrections.

coefficients (CCs) (*12*). On the southeast side of the epicenter, waveforms from the mainshock and the EGF exhibited high similarity (CCs > 0.85) at several Australian stations (e.g., AU.GVL, AU.STKA; Fig. 4C). On the southwest side, Mach waves were observed at stations in South Africa and Madagascar (e.g., II.SUR, II.ABPO; Fig. 4C). The Mach angle was 30° to 60°, which, assuming a local S wave speed (V_s) of 3.2 km/s, suggests a rupture speed of 3.4 to 5.8 km/s. This range is consistent with the rupture speed measured by SEBP, though minor uncertainties may arise from V_s variations, rupture complexity, and rupture speed fluctuations.

Theoretical analyses and laboratory experiments (*23*, *24*) have shown that a key characteristic of supershear ruptures is a dominant fault-parallel (FP) component in the near-fault ground velocity field, which exceeds the fault-normal (FN) component. This FP dominance has been observed in several reported supershear events, including the 2002 Denali, 2020 Caribbean, and 2023 Türkiye earthquakes (*25*–*29*). The seismic station GE.NPW, located 2 to 3 km from the fault trace (Fig. 2, A and B), recorded ground accelerations during the mainshock. After integrating the acceleration to velocity and removing the drift (*30*), we observed a larger peak ground velocity in the FP direction (~160 cm/s) than in the FN direction (~120 cm/s) (Fig. 2D). This amplitude pattern is consistent with the aforementioned supershear signature. Recent observations on the 2023 Türkiye earthquake (*31*) showed that a rupture propagating at 3 km/s could also generate the FP dominance, with this speed exceeding the V_s of 2.83 km/s in their model. Dynamic simulations (*32*) further demonstrated that an FP/FN > 1 indicates supershear rupture once the front stabilizes after the transition, though this ratio may fluctuate if the rupture front remains unsteady immediately following the supershear onset. To provide further constraint on rupture speeds, we integrated the acceleration waveforms twice to obtain displacement time series (Fig. 2E). Near-fault displacement records are known to be sensitive to slip on nearby fault segments (*33*). We identified the onset of significant horizontal ground displacement and interpreted it as the approximate arrival of the rupture front at the fault patch near the station. Motions in the N-S component began as early as ~50 s (Fig. 2E and fig. S29), corresponding to an estimated rupture speed of 4.9 km/s, given the station's epicentral distance of 246 km. This represents a lower bound on the average rupture velocity from the hypocenter, as we ignored undetectable fault slip, the 2- to 3-km distance from the fault to the station, and the vertical rupture propagation within the fault. Taken together, these complementary observations, including SEBP imaging, far-field Mach wave detection, near-field amplitude characteristics, and displacement-based rupture timing, collectively support the existence of a fast-propagating supershear rupture along the southern segment of the fault.

Supershear ruptures controlled by bimaterial effect, energy ratio, and fault geometry

The 2025 Mandalay earthquake exhibited two remarkable features: an exceptionally early transition to supershear rupture and a prolonged supershear propagation spanning at least 400 km, making it one of the longest documented supershear earthquakes to date. Several mechanisms have been proposed to explain supershear transition, i.e., how rupture accelerates to the supershear regime. The classic Burridge-Andrews mechanism (*34*, *35*) suggests that the rupture front at a sub-Rayleigh speed is preceded by a daughter crack, whose speed is the S wave speed at the beginning and accelerates to a stable supershear speed after a certain distance. Given a high initial shear stress and/or a weak fault, rupture can also directly transition to the supershear regime before apparent formation of a daughter crack (*36*). In addition to the assumption of uniform properties, the heterogeneities of fault strength and stress (*36*–*38*), free surface (*39*), fault roughness, curvature, or bending (*40*, *41*), fault step-overs (*42*), damage zones (*43*), and bimaterial effects (*44*–*46*) may also promote supershear transition. The southern segment of the Mandalay earthquake shared several similarities with the 2018 M_w 7.5 Palu event but exhibited a higher rupture speed (5 km/s compared with 4.1 km/s in the Palu event). This exceptionally long and fast rupture offers a valuable opportunity to assess theoretical and numerical models of supershear propagation.

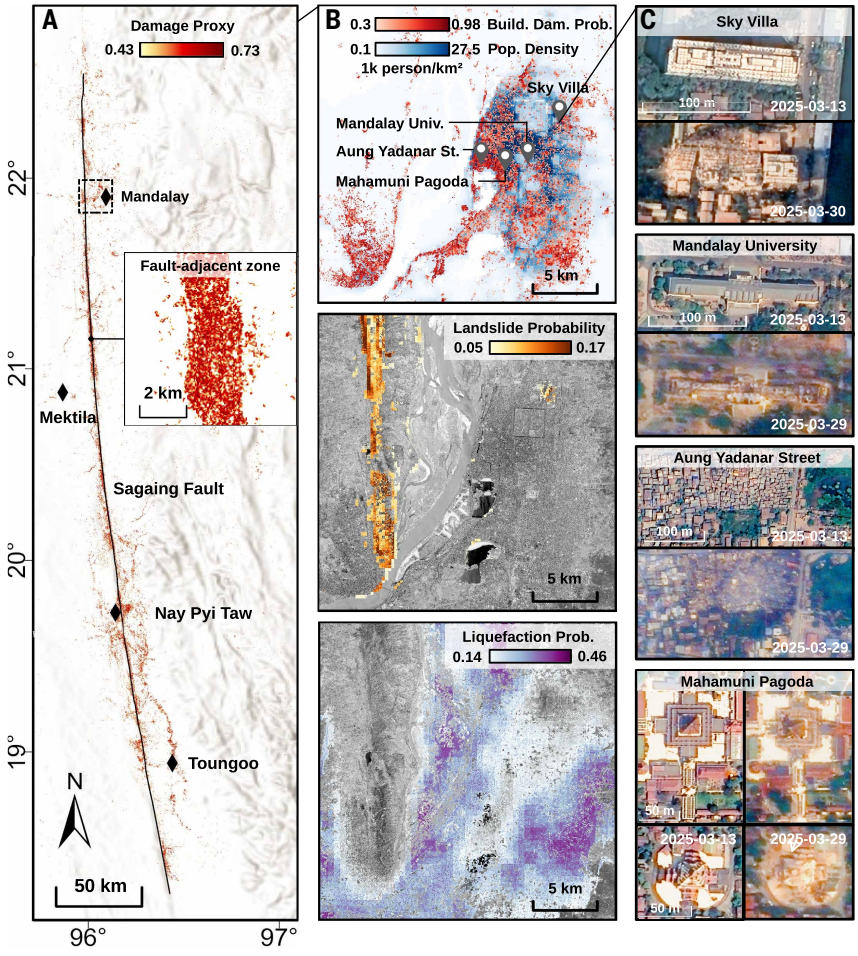

Fig. 3. Multihazard analysis of the earthquake region along the Sagaing fault. (**A**) DPM with white-to-red scale indicating increasing damage probability along the fault. (Inset) An enlarged view of a high-DPM zone near the fault. (**B**) Hazard probability distribution in Mandalay (light-to-dark scale), including building damage (top), landslides (middle), and liquefaction (bottom). Background layers show population density (white-to-blue scale) and Gaofen-1 optical imagery. (**C**) Damage interpretation in Mandalay derived from Jilin-1 optical imagery.

The Sagaing fault separates the Central Myanmar Basin to the west from Shan-Thai Block to the east (figs. S30 and S31). The former is characterized by a thick (~15 km) low-velocity layer consisting of Cenozoic basin sediments, and the latter features granite and the Mogok metamorphic belts with minimal sediment cover (*5*, *47*). The V_s structure along the Sagaing fault (*5*) reveals a pronounced material contrast across the fault within the shallowest 10 km, where most coseismic slip occurred. The eastern side exhibits V_s values of 2.8 to 3.7 km/s, whereas the western side shows lower V_s values of 2.2 to 3.3 km/s. By estimating the average velocity within the top 10 km as $V_{s\_mean}=10/\Sigma(dz/V_s)$, we obtained a V_{s_mean} of 2.9 and 3.3 km/s for the western and eastern sides, respectively. The difference in V_s suggests a difference in rock stiffness (*48*), a bimaterial contrast that influences rupture speed (*44*–*46*, *49*). Given the right-lateral strike-slip nature of the Sagaing fault, the southward rupture propagated in the negative direction, i.e., the moving direction of the stiff medium. Laboratory experiments and numerical simulations have shown that, in this direction, normal stress initially increases behind the rupture tip and decreases ahead of it. As the rupture propagates, the normal stress reduction becomes more pronounced, causing a broader region ahead of the rupture tip to yield simultaneously and accelerating the rupture to supershear speed. Once the rupture reaches supershear, the normal stress perturbation behind the crack tip reverses and becomes extensional rather than compressional (*44*–*46*, *50*). Conversely, rupture propagating in the positive direction (the moving direction of compliant medium) tends to experience increased normal stress ahead of the rupture tip, which favors subshear or nonsustained supershear behavior, explaining the slow rupture observed along the northern segment. However, dynamic simulations also predict a longer rupture extension in the positive direction compared with that in the negative direction (*51*, *52*), contrasting with the shorter northern branch of the Mandalay earthquake. This discrepancy could be explained by the five $M \geq 6.8$ events that occurred in the north between 1946 and 2012, which reduced stress accumulation (*2*) (Fig. 1A, table S3).

The observed rupture speed of 5 km/s was anomalously fast, corresponding to rupture speed/shear wave speed (V_r/V_s) ratios of 1.6 to 1.8, exceeding the Eshelby speed of $\sqrt{2} * V_s$ expected for rupture in a homogeneous medium (*53*). It also surpassed the predicted upper limit—the compliant side's compressional wave speed (V_p)—suggested by numerical simulations for the material contrast level across the Sagaing fault [$V_{s\_compliant}/V_{s\_stiff} = 0.85$; (*46*, *50*)] (fig. S31). These observations imply that factors beyond the bimaterial effect may have also contributed to the extreme rupture acceleration. One potential contributor is the poroelastic effect. Along the bimaterial Sagaing fault, the compliant side consists of porous sedimentary rocks, whereas the stiffer side comprises less porous metamorphic rocks (*54*). This material contrast could enhance the bimaterial effect and further promote rupture acceleration (*55*). Additionally, an elevated stress level due to the long period of seismic quiescence as well as the free-surface effect (*39*, *56*) may have played roles. Near-fault investigations, including mapping of distributed deformation, rock sampling from boreholes, and cross-fault seismic reflection experiments, will help evaluate these possibilities.

The ratio between the dissipated and potential energies (G_c/G_0) is another key factor controlling rupture propagation (*57*). Here, G_c represents the fracture energy dissipated near the rupture front, whereas G_0 denotes the static elastic energy release rate for strike-slip rupture with a finite rupture width (*12*). Theory and numerical simulations have demonstrated that persistent supershear propagation is permitted when $G_c/G_0 < 0.7$ is satisfied on a purely strike-slip fault (*57*). The southern segment of the Sagaing fault, between Mandalay and NayPyiDaw, has remained seismically quiescent without experiencing any $M \geq 7$ earthquakes since 1839 (Fig. 1A) (*2*). This prolonged interseismic period results in considerable prestress accumulation and slip deficit. Because G_0 depends more strongly than G_c on slip deficit (*12*, *56*), the energy ratio G_c/G_0 decreases with longer interseismic intervals. Thus, the extended seismic quiescence led to another favorable condition for sustained supershear rupture.

Fault geometry also has an important influence on earthquake rupture propagation. We found that the southern segment of the Sagaing fault exhibits a remarkably simple and linear geometry, which is conducive to persistent supershear propagation (*58*). The three-segment fault model used in the joint FFI incorporated a total strike variation of only 9° (Fig. 2). From the epicenter to (21.51°N, 95.99°E), the first segment extends ~55 km with a strike of 179°. The following 110-km segment to the south adopts a strike of 176°, and then the strike shifts

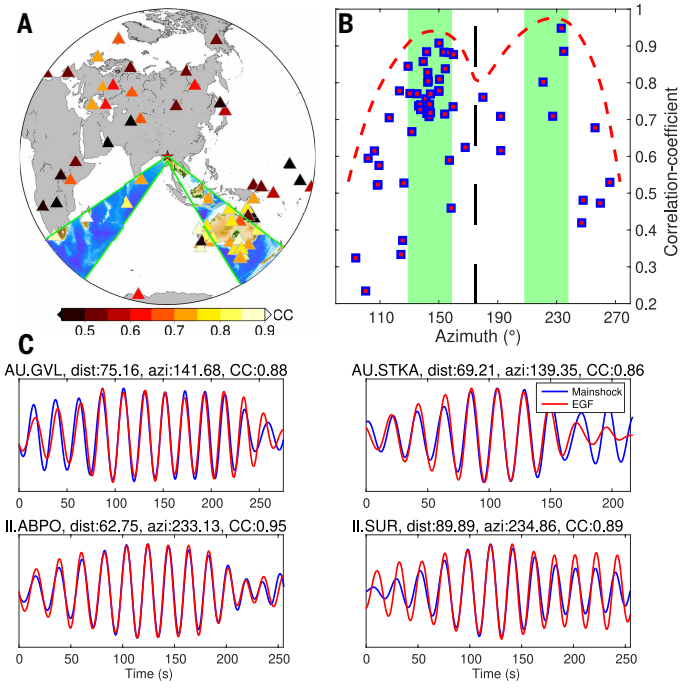

Fig. 4. Far-field Rayleigh wave Mach cones and waves. (**A**) Mach cone distribution. Colored areas within the green boundaries mark the Mach cones, where Mach waves have been identified. Seismic station locations are shown as triangles, with color indicating the CCs between 15- and 25-s Rayleigh wave displacement seismograms from the M_w 7.8 Mandalay mainshock and the M_w 5.1 EGF event. (**B**) Azimuthal distribution of waveform similarity. CCs between 15- and 25-s Rayleigh waveforms of the mainshock and EGF, plotted as a function of station azimuth. The black dashed line marks the rupture direction of the southern segment. Green bands denote the azimuthal extent of the identified Mach cones, accounting for uncertainties in Rayleigh wave phase and rupture velocities. The red dashed curve indicates the envelope that delineates the distribution pattern of CCs. (**C**) Representative Mach waves. Bandpass-filtered vertical displacement Rayleigh wave seismograms for the mainshock (blue) and EGF (red) at selected stations. Station name, azimuth (azi), and epicentral distance (dist; in degrees) are annotated.

to 172° for the next 220 km. Near the southern terminus, the strike rotates slightly to 170°. Whereas this three-segment model is a simplified representation of the fault based on ground deformation (Fig. 2B), detailed inspection of the surface trace indicates that the curve of the fault is continuous without any sizeable kinks or step-overs (fig. S32). Numerical simulations and laboratory experiments by (*59*, *60*) demonstrated that ruptures can propagate at supershear speeds across fault bends of 10°, whether on the extensional or compressional side, without any reduction in propagation velocity. Therefore, the geometrically simple and linear structure of the Sagaing fault likely helped to sustain supershear rupture propagation, consistent with observations in other large events (*58*).

REFERENCES AND NOTES

1. P. Bird, *Geochem. Geophys. Geosyst.* **4**, 2001GC000252 (2003).
2. Y. Wang, K. Sieh, S. T. Tun, K.-Y. Lai, T. Myint, *J. Geophys. Res. Solid Earth* **119**, 3767–3822 (2014).
3. G. Bertrand *et al.*, *C. R. Acad. Sci. II* **7**, 479–484 (1998).
4. C. Vigny *et al.*, *J. Geophys. Res.* **108** (B11), 2002JB001999 (2003).
5. X. Wang *et al.*, *J. Geophys. Res. Solid Earth* **124**, 504–526 (2019).
6. Z. Peng *et al.*, Mainshock rupture properties, aftershock activities and remotely triggered seismicity associated with the 2025 Mw 7.7 Sagaing Fault earthquake in Myanmar. EarthArXiv X5BQ7D (2025); https://doi.org/10.31223/X5BQ7D.
7. L. Meng, A. Zhang, Y. Yagi, *Geophys. Res. Lett.* **43**, 628–636 (2016).
8. C. Ji, D. J. Wald, D. V. Helmberger, *Bull. Seismol. Soc. Am.* **92**, 1192–1207 (2002).
9. G. Shao, X. Li, C. Ji, T. Maeda, *Earth Planets Space* **63**, 559–564 (2011).
10. S.-H. Yun *et al.*, *Seismol. Res. Lett.* **86**, 1549–1556 (2015).
11. Z. E. Ross *et al.*, *Science* **366**, 346–351 (2019).
12. Materials and methods are available as supplementary materials.
13. L. Xu *et al.*, *J. Geophys. Res. Solid Earth* **128**, e2022JB025936 (2023).
14. D. Melgar, G. P. Hayes, *Geophys. Res. Lett.* **44**, 9691–9698 (2017).
15. D. Wang, J. Mori, K. Koketsu, *Earth Planet. Sci. Lett.* **440**, 115–126 (2016).
16. L. Ye *et al.*, *Earth Planet. Sci. Lett.* **401**, 215–226 (2014).
17. L. Xu *et al.*, *Commun. Earth Environ.* **4**, 379 (2023).
18. L. T. Aung *et al.*, The 2012 Mw 6.8 Thabeikkyin earthquake in central Myanmar: A widely felt strong event with unilateral rupture through the Singu basalt on the Sagaing fault." in AGU Fall Meeting, 12 to 16 December 2022, Chicago, IL (AGU, 2022).
19. Y. Yang *et al.*, *Int. J. Appl. Earth Obs. Geoinf.* **133**, 104133 (2024).
20. S. Xu, J. Dimasaka, D. J. Wald, H. Y. Noh, *Nat. Commun.* **13**, 7793 (2022).
21. M. Vallée, E. M. Dunham, *Geophys. Res. Lett.* **39**, L05311 (2012).
22. H. Bao *et al.*, *Nat. Geosci.* **12**, 200–205 (2019).
23. M. Mello, H. S. Bhat, A. J. Rosakis, *J. Mech. Phys. Solids* **93**, 153–181 (2016).
24. V. Rubino, A. J. Rosakis, N. Lapusta, *J. Geophys. Res. Solid Earth* **125**, e2019JB018922 (2020).
25. E. M. Dunham, R. J. Archuleta, *Bull. Seismol. Soc. Am.* **94** (6B), S256–S268 (2004).
26. H. Bao *et al.*, *Nat. Geosci.* **15**, 942–949 (2022).
27. M. Abdelmeguid *et al.*, *Commun. Earth Environ.* **4**, 456 (2023).
28. C. Ren *et al.*, *Science* **383**, 305–311 (2024).
29. A. Rosakis, M. Abdelmeguid, A. Elbanna, *Nat. Geosci.* **18**, 534–541 (2025).
30. D. M. Boore, *Bull. Seismol. Soc. Am.* **91**, 1199–1211 (2001).
31. B. Delouis, M. van den Ende, J.-P. Ampuero, *Bull. Seismol. Soc. Am.* **114**, 726–740 (2023).
32. S. Yao, H. Yang, *Sci. Adv.* **11**, eadq0154 (2025).
33. H. Kanamori, E. E. Brodsky, *Rep. Prog. Phys.* **67**, 1429–1496 (2004).
34. R. Burridge, *Geophys. J. Int.* **35**, 439–455 (1973).
35. D. J. Andrews, *J. Geophys. Res.* **81**, 5679–5687 (1976).
36. Y. Liu, N. Lapusta, *J. Mech. Phys. Solids* **56**, 25–50 (2008).
37. E. M. Dunham, P. Favreau, J. M. Carlson, *Science* **299**, 1557–1559 (2003).
38. J. N. Hayek *et al.*, *Geophys. Res. Lett.* **51**, e2024GL110128 (2024).
39. Y. Kaneko, N. Lapusta, *Tectonophysics* **493**, 272–284 (2010).
40. L. Bruhat, Z. Fang, E. M. Dunham, *J. Geophys. Res. Solid Earth* **121**, 210–224 (2016).
41. X. Ma, A. Elbanna, *Earth Planet. Sci. Lett.* **523**, 115702 (2019).
42. K. J. Ryan, D. D. Oglesby, *J. Geophys. Res. Solid Earth* **119**, 5814–5829 (2014).
43. Y. Huang, J. P. Ampuero, D. V. Helmberger, *Earth Planet. Sci. Lett.* **433**, 109–115 (2016).
44. S. Langer, L. Olsen-Kettle, D. Weatherley, *Geophys. J. Int.* **190**, 1169–1180 (2012).
45. H. Shlomai, J. Fineberg, *Nat. Commun.* **7**, 11787 (2016).
46. H. Shlomai, M. Adda-Bedia, R. E. Arias, J. Fineberg, *J. Geophys. Res. Solid Earth* **125**, e2020JB019829 (2020).
47. A. Mitchell, The Shan Plateau West of the Salween, *Geological Belts, Plate Boundaries, and Mineral Deposits in Myanmar*, A. Mitchell, Ed. (Elsevier, 2018), pp. 19–76.
48. D. Boore, *Bull. Seismol. Soc. Am.* **106**, 316–320 (2016).
49. K. Xia, A. J. Rosakis, H. Kanamori, J. R. Rice, *Science* **308**, 681–684 (2005).
50. Z. Shi, Y. Ben-Zion, *Geophys. J. Int.* **165**, 469–484 (2006).
51. M. Abdelmeguid, A. Elbanna, *Earth Planet. Sci. Lett.* **593**, 117648 (2022).
52. D. J. Andrews, Y. Ben-Zion, *J. Geophys. Res.* **102** (B1), 553–571 (1997).
53. K. Xia, A. J. Rosakis, H. Kanamori, *Science* **303**, 1859–1861 (2004).
54. Z. Zhou *et al.*, *J. Oceanol. Limnol.* **42**, 1074–1086 (2024).
55. E. M. Dunham, J. R. Rice, *J. Geophys. Res.* **113** (B9), 2007JB005405 (2008).
56. J. Xu, H. Zhang, X. Chen, *Geophys. J. Int.* **202**, 2194–2206 (2015).
57. H. Weng, J. P. Ampuero, *Nat. Geosci.* **13**, 817–821 (2020).
58. M. Bouchon *et al.*, *Tectonophysics* **493**, 244–253 (2010).
59. C.-E. Rousseau, A. J. Rosakis, *J. Geophys. Res.* **108** (B9), 2002JB002310 (2003).
60. E. L. Templeton *et al.*, *J. Geophys. Res.* **114** (B8), 2008JB006174 (2009).
61. R. Burns, piyushrpt, Z. Yunjun, B. Marfito, C. Liang, H. Fattahi, E. Fielding, Microwave Remote Sensing Laboratory, G. Manipon, S. Mirzaee, S. Staniewicz, Andy CA6JAU, V. Schut, asolarte, mzzhong, dbekaert, S. S. Sangha, Russell, G. H. X. Shiroma, L. Zhu, shitong01, hbparache, J. H. Kennedy, F. Amelung, bbuzz31/isce2: Buzzanga et al., 2023, (v2.6.3), Zenodo (2023); https://doi.org/10.5281/zenodo.8157051.
62. L. Xu, Z. Yunjun, Y. Yang, Y. Wang, C. Hu, Geodetic Deformation, DPM products, and source imaging results in "Bimaterial Effect and Favorable Energy Ratio Enabled Supershear Rupture in the 2025 Mandalay Earthquake", Zenodo (2025); https://doi.org/10.5281/zenodo.17113746.
63. L. Xu, L. Meng, Codes for Slowness-Enhanced Back-Projection (SEBP), Zenodo (2024); https://doi.org/10.5281/zenodo.12801968.
64. U.S. Geological Survey, Earthquake Hazards Program, Advanced National Seismic System (ANSS) Comprehensive Catalog of Earthquake Events and Products: Various (2017); https://doi.org/10.5066/F7MS3QZH.
65. G. Ekström, M. Nettles, A. M. Dziewonski, *Phys. Earth Planet. Inter.* **200-201**, 1–9 (2012).

66. R. Newman *et al.*, Wilber 3: A Python-Django Web Application For Acquiring Large-scale Event-oriented Seismic Data, Incorporated Research Institutions for Seismology (2013); https://ds.iris.edu/wilber3/.
67. A. Strollo *et al.*, *Seismol. Res. Lett.* **92**, 1788–1795 (2021).
68. GEOFON Data Centre, GEOFON Seismic Network (GFZ Helmholtz Centre for Geosciences, 1993). https://doi.org/10.14470/TR560404.
69. M. Beyreuther *et al.*, *Seismol. Res. Lett.* **81**, 530–533 (2010).
70. WorldPop, WorldPop Global Project Population Data; https://hub.worldpop.org/.
71. U.S. Geological Survey, Earthquake Hazards Program; https://earthquake.usgs.gov/earthquakes/eventpage/us7000pn9s/ground-failure/about.
72. Changguang Satellite, Jilin-1 Repository; https://www.jl1mall.com/resrepo/.
73. D. Gansu, *RSC: Comparative Analysis Data Before and After the Myanmar Earthquake on March 28, 2025* (National Tibetan Plateau / Third Pole Environment Data Center, 2025).
74. P. Wessel, W. H. F. Smith, *Eos* **79**, 579 (1998).
75. R. B. Lohman, W. D. Barnhart, *J. Geophys. Res. Solid Earth* **115**, 12413 (2010).

ACKNOWLEDGMENTS

We thank reviewer M. Abdelmeguid and the two anonymous reviewers for their constructive comments. We thank China Earthquake Networks Center (CENC) for providing the aftershock catalog. We thank Y. Wang for providing the fault dataset of Myanmar. We thank the US Geological Survey for providing Sentinel-2 and surface rupture data. We thank the European Space Agency, China Centre for Resources Satellite Data and Application, and Aerospace Exploration Agency for providing the Sentinel-1, LuTan-1, and ALOS-2 SAR imagery. We thank Google Maps for providing topography and world street maps. **Funding:** This work is supported by the NSF grant EAR-2506181 (L.X., L.M.) and the National Natural Science Foundation of China grants 42388102 and 42174023 (W.X.). **Author contributions:** Conceptualization: L.M., C.J., Z.Y., L.X.; Methodology: L.X., C.J., L.M., Z.Y., Y.Y.; Investigation: L.X., Z.Y., Y.Y., Y.W., C.H., H.W., C.J., E.S.; Visualization: L.X., Z.Y., Y.Y., Y.W., C.H., W.X.; Supervision: L.M., C.J., Z.Y.; Writing – original draft: L.X., H.W., Z.Y., C.J., Y.Y.; Writing – review & editing: all authors. **Competing interests:** The authors declare that they have no competing interests. **Data and materials availability:** All data are available in the main text or the supplementary materials. The SAR processing is performed using the ISCE-2 software, available at (*61*). The geodetic dataset, DPM products, and source imaging results of this study are available at (*62*). The MATLAB code for SEBP is available at (*63*). The moment tensor solutions came from the USGS (http://earthquake.usgs.gov) (*64*) and the Global Centroid Moment Tensor project (http://www.globalcmt.org) (*65*). All teleseismic data can be downloaded through the IRIS Wilber 3 system (https://ds.iris.edu/wilber3/) (*66*) and ORFEUS (www.orfeus-eu.org) (*67*). The local strong motion data can be downloaded from IRIS Wilber 3 system (https://ds.iris.edu/wilber3/) (*66*) and GFZ Helmholtz Centre for Georesearch (https://geofon.gfz.de/) (*68*). The Python software package Obspy (www.obspy.org) (*69*) was used for seismic data requesting and waveform filtering. Some of the images in the figures were based on optical images from Google Map, World Hillshade, OpenStreetMap, Jilin-1, and GaoFen series of satellites. Population density data was from the WorldPop Global Project Population Data (https://hub.worldpop.org/) (*70*). The hazard model and fault traces data are available on USGS (https://earthquake.usgs.gov/earthquakes/eventpage/us7000pn9s/executive) (*71*). The Jilin-1 imagery source is available at https://www.jl1mall.com/resrepo/ (*72*). The Gaofen series datasets are provided by National Tibetan Plateau/Third Pole Environment Data Center (http://data.tpdc.ac.cn) (*73*). Figures were produced using Generic Mapping Tools (*74*), Obspy, and Matlab. The static displacement data was downsampled by InSamp (https://github.com/williamBarnhart/InSamp) (*75*).

SUPPLEMENTARY MATERIALS

science.org/doi/10.1126/science.ady6100
Materials and Methods; Figs. S1 to S40; Tables S1 to S6; References (*76*–*118*); Movies S1 to S4

Submitted 28 April 2025; accepted 8 September 2025

10.1126/science.ady6100